

Molecular-dynamics study of diffusional creep in uranium mononitride

Mohamed AbdulHameed^a, Benjamin Beeler^{a,b,*}, Conor O.T. Galvin^d, Michael W.D. Cooper^d, Nermene Elamrawy^a, Antoine Claisse^c

^a*Department of Nuclear Engineering, North Carolina State University, Raleigh, NC 27695*

^b*Idaho National Laboratory, Idaho Falls, ID 83415*

^c*Westinghouse Electric Sweden, Västerås, SE 72163, Sweden*

^d*Los Alamos National Laboratory, Los Alamos, NM 87545*

Abstract

Uranium mononitride (UN) is a promising advanced nuclear fuel due to its high thermal conductivity and high fissile density. Yet, many aspects of its mechanical behavior and microstructural features are currently unknown. In this paper, molecular dynamics (MD) simulations are used to study UN's diffusional creep. Nanometer-sized polycrystals are used to simulate diffusional creep and to calculate an effective GB width. It is found that Nabarro-Herring creep is not dominant in the temperature range of 1700–2000 K and that the dominant diffusional creep mechanism is Coble creep with an activation energy of 2.28 ± 0.09 eV. A method is proposed to calculate the diffusional GB width and its temperature dependence in polycrystals. The effective GB width of UN is calculated as 2.69 ± 0.08 nm. This value fits very well with the prefactor of the phenomenological Coble creep formula. It is demonstrated that the most comprehensive thermal creep model for UN can be represented as the combination of our Coble creep model and the dislocation creep model proposed by Hayes *et al.*

Keywords: [..¹]Uranium nitride, [..²]Molecular dynamics, Coble creep, Nabarro-Herring creep, [..³]Grain-boundary width, [..⁴]Grain-boundary diffusion

*Corresponding author

Email address: bwbeeler@ncsu.edu (Benjamin Beeler)

¹removed: uranium

²removed: molecular

³removed: grain-boundary

⁴removed: grain-boundary

1 1. Introduction

Uranium mononitride (UN) is a potential next-generation nuclear fuel with several favorable properties like high fissile density, good heat transfer, compatibility with most potential cladding materials, and longer fuel residence periods [1–3]. However, it also has challenges like complex manufacturing processes, high cost due to ^{15}N enrichment, and vulnerability to steam at high temperatures [1–3]. Many aspects of the mechanical behavior and microstructural features of UN at high temperatures and under irradiation are lacking in both consistent experimental data and detailed mechanistic understanding. The mechanical properties of nuclear fuels are crucial for a better understanding of the pellet-cladding mechanical interactions (PCMI) that occur during reactor operation, where cladding creep-down and fuel swelling lead to contact and the development of stresses between the cladding and the fuel, which, with the build-up of fission products, promotes stress corrosion cracking in the cladding material [4]. Fuel creep has an important role in accommodating void swelling once the fuel contacts the cladding [2].

There are a limited number of experimental investigations into the creep behavior of UN. Hayes *et al.* [5] developed an empirical correlation for the steady-state thermal creep rate of UN based on three experimental investigations by Fassler *et al.* [6], Vandervoort *et al.* [7], and Uchida and Ichikawa [8]. These experiments were conducted at a temperature range of 1373–2083 K, a stress range of 13–55.1 MPa, and for five grain sizes: 9, 15, 30, 140, and 2000 μm . In addition, the tested samples contained varying levels of carbon and oxygen impurities. To determine the mechanism controlling the creep of UN, Hayes *et al.* [5] determined the average stress exponent, based only on the data by Fassler *et al.* [6] and Vandervoort *et al.* [7], to be $n = 4.5$. They therefore concluded that the dominant creep mechanism is most probably a climb-controlled dislocation glide mechanism, for which there is no grain size dependence, i.e., the grain size exponent $q = 0$. The data by Uchida and Ichikawa [8] gave a stress exponent $n = 1.8\text{--}2.6$, which is indicative of a combination between diffusional and dislocation creep. However, Hayes *et al.* decided to disregard this data set because its temperature range was intermediate between that of Fassler *et al.* [6] and Vandervoort *et al.* [7], and they deemed it was unlikely that a diffusion-based mechanism would only be active in such a narrow temperature range (i.e., 1583–1773 K). The rest of the correlation (i.e., the prefactor and the activation energy) was only fit to the data by Vandervoort *et al.* [7] because it is the only data set that reported stoichiometric samples of 100% theoretical density. The final correlation reads:

$$\dot{\epsilon} = 2.054 \times 10^{-3} \sigma^{4.5} \exp\left(-\frac{39369.5}{T}\right), \quad (1)$$

where $\dot{\epsilon}$ is the creep rate measured in s^{-1} , σ is the stress measured in MPa, and T is the temperature measured in K. The correlation is strictly valid for $T = 1770\text{--}2083$ K (although it was assumed by Hayes *et al.* to yield reasonable estimates of the creep rate over the range of 298–2523 K), $\sigma = 20\text{--}34$ MPa, and theoretically dense UN. The exponential term in Eq. (1) corresponds to an activation energy $Q = 3.39$ eV.

Rogozkin *et al.* [9] performed experiments and reported thermal creep data for $\text{U}_{0.8}\text{Pu}_{0.2}\text{N}$. They found that for theoretically dense samples, the thermal creep rate follows the corre-

41 tion:

$$\dot{\epsilon} = 27.7\sigma^{1.35} \exp\left(-\frac{40000}{T}\right), \quad (2)$$

42 which indicates an activation energy $Q = 3.45$ eV. The investigators noted that the mass
43 fraction of oxygen and carbon impurities did not exceed 0.15% and the stress varied from
44 10 to 60 MPa. However, they did not report any grain sizes or an explicit unit for the
45 creep rate. Note that a stress exponent of 1.35 in Eq. (2) is close to 1 and might indicate a
46 diffusion-dominant creep mechanism [9, 10].

47 Nabarro-Herring (N-H) creep of UN has been investigated via computational tools. Ko-
48 tomin *et al.* [11] conducted a DFT investigation of the diffusion mechanisms of U and N
49 atoms in UN and calculated their associated migration energies. Assuming thermal creep
50 is rate-limited by the diffusion of the slower species (i.e., uranium), they concluded that
51 the activation energy of thermal creep in bulk UN is 5.6 eV. Their thermal creep model is
52 incorporated into the TRANSURANUS fuel performance code [11].

53 Finally, Konovalov *et al.* [12] conducted a compilation of available data on UN, (U, Pu)N,
54 UC, and mononitrides of refractory metals (e.g., Zr and Ti) to find a correlation for thermal
55 and irradiation creep in UN and (U, Pu)N. Based on the data, they assumed a combination
56 of dislocation-climb creep and Coble creep according to:

$$\dot{\epsilon} = a_1\sigma^n \exp\left(-\frac{Q_b}{k_B T}\right) + fa_2\frac{\sigma}{k_B T} \exp\left(-\frac{Q_{GB}}{k_B T}\right), \quad (3)$$

57 where a_1 and a_2 are estimated from typical values for refractory-metal mononitrides, the
58 stress exponent of the dislocation-climb creep part is $n = 4.5$, the same as in Eq. (1), and
59 f is the volume fraction of GBs. Note that the dependence of the Coble creep on the grain
60 size is included in a_2 . They further assumed that the activation energy for the dislocation-
61 climb creep is equal to the activation energy of bulk diffusion of U atoms in UN, i.e., $Q_b =$
62 5 eV. Based on the observation that in typical metallic compounds, the activation energy
63 of GB diffusion is nearly half that of bulk diffusion, they assumed $Q_{GB} = 0.53Q_b$, similar
64 to UC, because measurements of U self-diffusion at GBs in UN are not yet available. An
65 important result of their analysis is that diffusional creep is the dominant mechanism in the
66 temperature range of fuel manufacturing processes and nuclear reactor operation, although
67 they did not clarify the effect of stress and grain size.

68 A few observations can be made about the previous studies. The assumption by Hayes
69 *et al.* that dislocation creep is the dominant creep process cannot be made for all grain sizes
70 at all temperatures based only on very few experimental data points. The studies by Fassler
71 *et al.* [6] and Vandervoort *et al.* [7], on which the stress exponent in Eq. (1) was based,
72 report grain sizes of 30, 140, and 2000 μm . However, typical grain sizes of manufactured
73 UN fuel range between 5 and 30 μm [13–16]. Johnson and Lopes [14] report that the grain
74 size for UN to achieve optimum fuel porosity (i.e., 0% open porosity to suppress oxidation
75 and 4% closed porosity to accommodate gas fission products) is around $8 \pm 1 \mu\text{m}$. Uchida
76 and Ichikawa [8], who found a stress exponent closer to 1, reported grain sizes of 9 and
77 15 μm . That is, diffusional creep might be the dominant creep mechanism at the grain
78 sizes typical of the manufactured fuel. The existence of diffusional creep as a contributing
79 process is supported by the studies of Rogozkin *et al.* [9] and Konovalov *et al.* [12], and can

80 be dominant if the activation energy of a diffusional creep mechanism is found to be lower
81 than that of dislocation creep. Basing the thermal creep model of UN on bulk diffusion
82 activation energies, as was done by Kotomin *et al.* [11], is questionable, especially because
83 GB diffusion is known to be much faster than bulk diffusion [17], and the typical grain sizes of
84 manufactured UN (5–30 μm) are quite small and might render Coble creep as the dominant
85 mechanism at the temperature range of practical interest. Finally, Nabarro-Herring creep is
86 expected to be dominant near the melting point [18].

87 It is worth mentioning that Hayes *et al.* [19] also developed correlations for diffusion in
88 UN based on a few scattered data points. Their estimated activation energies for U and N
89 atoms are 0.69 and 1.66 eV, respectively, which raises suspicions because U atoms are not
90 expected to have a lower diffusion activation energy than that of N atoms. Hayes *et al.*
91 reported that their correlation for N diffusion is for tracer diffusion measurements, and is
92 only representative of extremely hyper-stoichiometric conditions. Finally, while the analysis
93 by Konovalov *et al.* [12] is qualitatively appealing, it lacks quantitative insights because
94 it is based on typical values and educated guesses. In summary, the literature on creep in
95 UN is sparse, somewhat contradictory, and requires additional investigation to identify the
96 dominant creep mechanisms at various temperatures, stresses, and grain sizes.

97 Molecular-dynamics (MD) studies have been used with success to study diffusional creep
98 in, e.g., Si [20], Pd [21], and $[\dots^5 \text{UO}_2]$ [22, 24]. These studies set up a simulation for idealized
99 microstructures, where the supercells are equilibrated at a certain temperature and put
100 under stress, and the strain rate is then analyzed. Haslam *et al.* [25] further developed this
101 approach by using random grain sizes and shapes, instead of idealized microstructures, to
102 observe both creep rate and grain growth mechanisms in Pd. Cooper *et al.* [26] used another
103 approach (hereafter termed the parameter-based approach) for predicting Coble creep rates
104 for $[\dots^6 \text{U}_3\text{Si}_2]$ where, instead of directly observing creep, an initial creep formula is assumed,
105 and then, a lower-length scale modeling approach is used to calculate the formula parameters,
106 e.g., defect volumes and GB diffusivities. To the best of our knowledge, no computational
107 studies exist in the literature for Coble creep in UN.

108 In order to conduct MD simulations, a sufficiently accurate interatomic potential is re-
109 quired. Two promising interatomic potentials of UN exist in the literature: Tseplyaev and
110 Starikov's angular-dependent potential [27], and Kocevski *et al.*'s embedded-atom method
111 (EAM) potential [28]. Both potentials have been utilized and compared in our previous
112 works [29, 30], however, their ability to model dynamical processes like diffusional creep has
113 not been assessed. In this work, nano-sized polycrystals are employed to perform MD simu-
114 lations of diffusional creep in UN. The polycrystals are also used to study GB diffusion and
115 the temperature dependence of the diffusional GB width in UN. A parameter-based model
116 of Coble creep is also constructed and compared to the simulation model.

117 2. Methods

118 All MD calculations performed in this work utilize the Large-scale Atomic/Molecular
119 Massively Parallel Simulator (LAMMPS) software package [31] using a 1 fs time step and

⁵removed: UO_2 [22, 23]

⁶removed: U_3Si_2

¹²⁰ the Tseplyaev [27] and Kocevski [28] force-field potentials. Periodic boundary conditions
¹²¹ (PBCs) are applied to all supercells. The Atomsk code [32] is used to generate polycrystals
¹²² by the Voronoi tessellation method. The OVITO software package [33] is used for supercell
¹²³ visualization and analysis.

¹²⁴ *2.1. Creep mechanisms*

¹²⁵ Steady-state creep strain rates can be represented by the Mukherjee-Bird-Dorn equation
¹²⁶ [34]:

$$\dot{\epsilon} = \frac{A}{T} \frac{\sigma^n}{d^q} \exp\left(-\frac{Q}{k_B T}\right) \approx C \frac{\sigma^n}{d^q} \exp\left(-\frac{Q}{k_B T}\right), \quad (4)$$

¹²⁷ where T is temperature, σ is stress, d is the grain size, Q is an activation energy, ^{[..⁷] k_B} is the
¹²⁸ Boltzmann constant, and A , n , and q are dimensionless constants. The inverse temperature
¹²⁹ dependence A/T is relatively weak, especially at temperatures where creep is important,
¹³⁰ and is usually neglected [35]. That is why $A/T \approx C$ is treated as a constant prefactor. The
¹³¹ values of the exponents n and q depend on the creep mechanism under consideration. For
¹³² example, for power-law (dislocation) creep, $n = 3-8$ and $q = 0$, i.e., no grain size dependence,
¹³³ whereas for diffusional creep, $n = 1$ and $q = 2$ (for the Nabarro-Herring mechanism) or $q =$
¹³⁴ 3 (for the Coble mechanism).

¹³⁵ It should be noted that the Harper-Dorn creep, a dislocation creep mechanism, has a
¹³⁶ stress exponent $n = 1$, similar to diffusional-creep mechanisms, as well as $q = 0$, i.e., no
¹³⁷ grain size dependence. However, for Harper-Dorn creep to be significant, the material must
¹³⁸ have a large grain size (in the order of $100 \mu\text{m}$ [10]); otherwise, diffusional creep mechanisms
¹³⁹ are more likely to dominate. There is little evidence for the existence of Harper-Dorn creep in
¹⁴⁰ ceramics [10]. Ceramics generally have smaller grain sizes, fewer available slip systems, and
¹⁴¹ high Peierls-Nabarro stresses, all of which lead to the prevalence of other creep mechanisms
¹⁴² [10]. For this reason, the Harper-Dorn creep is excluded from consideration as a competing
¹⁴³ creep mechanism in UN, and dislocation creep refers exclusively to power-law creep.

¹⁴⁴ In this work, we study diffusional creep, whose rate, in general, is a sum of the Nabarro-
¹⁴⁵ Herring creep rate, $\dot{\epsilon}_{\text{NH}}$, and the Coble creep rate, $\dot{\epsilon}_C$, since both mechanisms operate in
¹⁴⁶ parallel [18].

¹⁴⁷ For Coble creep, the steady-state strain rate is expressed as [18, 36]:

$$\dot{\epsilon}_C = A_C \frac{\sigma \Omega}{k_B T} \frac{D_{\text{GB}} \delta}{d^3} \quad (5)$$

¹⁴⁸ where A_C depends on the grain shape ($A_C = 46.347$ for spherical grains), D_{GB} is the *effective*
¹⁴⁹ GB diffusivity, δ is the GB width, and Ω is the vacancy volume usually approximated as
¹⁵⁰ the atomic volume or expressed as b^3 [34] or $0.7b^3$ [10] where b is the magnitude of the
¹⁵¹ Burgers vector. In this formulation, $D_{\text{GB}} \delta$ is the diffusion flux in the GB, and $\sigma \Omega$ is the
¹⁵² work performed by the stress during an elementary diffusion jump [20, 21]. It should be
¹⁵³ noted that the original paper by Coble [36] reports the value of A_C for spherical grains as
¹⁵⁴ 148. However, we performed the derivation by Coble and found a value of $A_C = 46.347$.
¹⁵⁵ This agrees with the values of 47 reported by Kebinski *et al.* [20] and $148/\pi$ by Wang *et al.*

⁷removed: k_B

[37]. The maximum difference between these different results for A_C is only a factor of three; thus, it is effectively negligible compared to the orders of magnitude difference in creep rate resulting from, for example, d in Eq. (5). In Section 3.2, Eq. (5) is used as a basis for the parameter-based Coble creep model.

Homogeneous grain elongation along the tensile stress direction during diffusional creep requires GB sliding as a geometrically necessary accommodation process [18, 21]. In this context, GB sliding happens sequentially to diffusional creep on a local atom-by-atom basis and does not involve changes in the relative positions of the centers of mass of individual grains (i.e., their coordinates normalized by the simulation box dimensions are constant) [18]. If GB sliding were absent, voids/microcracks would form along the GBs. Since GB sliding and diffusional creep occur sequentially and sliding is faster than diffusion [18], the net creep rate is the rate of the slower process, which is diffusional creep.

2.2. Diffusional creep

High-temperature deformation and grain growth are coupled phenomena. Deformation enhances grain growth, and, in turn, grain growth can either *increase* or *decrease* the deformation rate depending on the interplay between the GB processes governing this coupling, which include GB diffusion, GB sliding, GB migration, and grain rotation [25]. Although the Coble creep formula (Eq. (5)) implies that grain growth reduces the creep rate, experimental evidence suggests that the strain rate can also increase during deformation due to GB migration, which acts as a stress-relaxation mechanism [25]. To suppress grain growth, an idealized nanocrystalline microstructure of uniform grain sizes and shapes is usually used in MD creep simulations [20, 21]. The geometry of grains can be closely modeled by the space-filling 14-sided polyhedron known as the truncated octahedron [21, 38]. Truncated-octahedral grains are nearly spherical, yet [..⁸] they display realistic grain features like triple lines and quadruple junctions. Atomsk [32] was used to generate 16 truncated-octahedral grains with random misorientations, and average grain diameters of 14, 16, 18, and 20 nm. Based on our tests, smaller grain sizes (10 and 12 nm) suffered inconsistent evolution in creep simulations at the highest temperature (i.e., 2000 K) and the lowest stress (i.e., 200 MPa). Random grain misorientations lead to a relatively small fraction of low-angle GBs [21, 25]; thus, all GBs within a polycrystal can be considered high-angle GBs. Atoms with distances smaller than $0.45a$, where a is the lattice parameter, were deleted to prevent [..⁹] unrealistically high forces as an artifact of the structure generation process.

Based on initial tests, we found that the Kocevski potential stabilizes voids along GBs in both bicrystals and polycrystals. This is likely due to the U-U repulsion in the Kocevski potential and its inability to simulate metallic U [29]. Thus, the Kocevski potential [..¹⁰] cannot be used for the study of Coble creep phenomena. [..¹¹] Additionally, governed by the migration of vacancies and atoms along GBs, accurate modeling of Coble creep requires reliable predictions of the energetics of vacancies and interstitials. The Tseplyaev potential provides accurate formation and migration energies for both stoichiometric and non-stoichiometric point

⁸removed: ,

⁹removed: unrealistic

¹⁰removed: is unable to

¹¹removed: For this reason

¹⁹⁵ defects that closely agree with DFT values [27, 29, 39]. On the other hand, the Kocevski potential
¹⁹⁶ fails to reproduce accurate formation energies for U-rich and stoichiometric conditions [29]. For
¹⁹⁷ these reasons, only the Tseplyaev potential is used to simulate the creep behavior of UN.

¹⁹⁸ Supercells are equilibrated in the *NPT* ensemble using the Nosé-Hoover thermostat and
¹⁹⁹ barostat at temperatures of 1700–2000 K and zero pressure for 200 ps. Then, tensile stresses
²⁰⁰ in the range of 200–500 MPa are applied to the supercells in the *x*-direction for 5 ns. The
²⁰¹ calculations were repeated using three different initial velocity distributions.

²⁰² Diffusional creep is typically observed for $T > 0.5T_m$, where T_m is the melting point [18].
²⁰³ For UN, the experimental melting temperature is about 3035 K at a nitrogen vapor pressure
²⁰⁴ of 1 atm [40], and the Tseplyaev potential predicts thermodynamic melting of UN at about
²⁰⁵ 2700 K [29]. Thus, diffusional creep is expected to be observed at the studied temperature
²⁰⁶ range of 1700–2000 K. On the other hand, the applied stresses (i.e., 200–500 MPa) are an
²⁰⁷ order of magnitude higher than typical experimental stresses at which creep is observed and
²⁰⁸ will lead to strain rates in the range of 10^6 s^{-1} , which is several orders of magnitude higher
²⁰⁹ than experimental creep rate values. However, such high stresses are required for creep to be
²¹⁰ observed within MD time scales. If we decrease the applied stress by an order of magnitude
²¹¹ and increase the grain size from 10 nm to 10 μm , the strain rate becomes 10^{-4} – 10^{-5} s^{-1} —
²¹² a typical experimental creep rate value. However, this would increase the computational
²¹³ cost to achieve a similar creep strain by approximately 10^4 times. It is expected that the
²¹⁴ fundamental physics of Coble creep is captured, given the computational setup applied here,
²¹⁵ and thus the extrapolation of conclusions from high stress/small grain simulations to more
²¹⁶ realistic stresses and grain sizes is considered reasonable. **Ultrahigh strain rates have been**
²¹⁷ **traditionally used in MD modeling of Coble creep and tensile testing [20–22, 25, 30].**

²¹⁸ To visualize the microstructural details of the supercells, the centrosymmetry parameter
²¹⁹ (CSP) and the dislocation extraction algorithm (DXA) are utilized. The CSP has been
²²⁰ calculated by OVITO for snapshots of the simulated supercells using the minimum-weight
²²¹ matching algorithm [41]. The CSP quantifies lattice disorder and is defined as [42]:

$$\text{CSP} = \sum_{i=1}^{N/2} |\mathbf{r}_i + \mathbf{r}_{i+N/2}|^2, \quad (6)$$

²²² where N represents the number of nearest neighbors around an atom (for NaCl, $N = 6$), and
²²³ \mathbf{r}_i and $\mathbf{r}_{i+N/2}$ are vectors extending from the atom in question to a pair of opposite neighbor-
²²⁴ ing atoms. In a perfectly centrosymmetric crystal, contributions from all neighboring pairs
²²⁵ cancel each other, yielding a CSP of zero. The CSP method is resilient to thermal noise;
²²⁶ for a pristine crystal, it produces a single peak starting at zero, with its width broadening
²²⁷ as temperature T increases. A second peak in the CSP graph indicates a different local
²²⁸ structure, such as dislocations or highly disordered grain boundaries (GBs) [41, 43]. The
²²⁹ CSP has units of squared distance, typically expressed as a^2 , where a is the lattice constant.
²³⁰ The CSP serves as an indirect analysis method. For direct visualization of dislocations,
²³¹ OVITO’s DXA [44] is used, particularly applied to the U sub-lattice. A drawback of the
²³² DXA is its limitation in identifying predefined dislocations in single-component crystals, so
²³³ dislocations with a Burgers vector outside the predefined families go undetected. This limits
²³⁴ the algorithm’s ability to identify GB dislocations, which typically have much shorter Burg-
²³⁵ ers vectors than those in the lattice [45]. Given that each sub-lattice in the B1 structure of

²³⁶ UN forms a face-centered cubic (FCC) lattice, applying DXA to the U sub-lattice allows for
²³⁷ precise dislocation identification and visualization.

²³⁸ 3. Results

²³⁹ 3.1. Direct simulation of Coble creep

²⁴⁰ A model microstructure of UN whose energy has been minimized at 0 K with a relative
²⁴¹ energy tolerance of 10^{-9} is shown in Fig. 1. The numbers of atoms in the constructed
²⁴² polycrystals range between 1,547,344 atoms for the 14-nm polycrystal and 4,537,943 atoms
²⁴³ for the 20-nm polycrystal, and the N/U ratio varies between 0.9999 and 1.0002. Each system
²⁴⁴ is therefore either slightly hypo-stoichiometric or slightly hyper-stoichiometric, and any effect
²⁴⁵ that may arise due to this slight off-stoichiometry is minor. Each creep rate is an average
²⁴⁶ over three simulations using three different initial velocity distributions. To visualize the GB
²⁴⁷ structure, atoms have been colored according to their CSP; yellow atoms have high CSP (i.e.,
²⁴⁸ high degree of miscoordination) and dark purple atoms have low CSP (i.e., low degree of
²⁴⁹ miscoordination). Conceptually, low-angle GBs consist of isolated dislocation cores of high
²⁵⁰ miscoordination that are separated by a nearly perfect crystal region of low miscoordination
²⁵¹ [46]. On the other hand, high-angle GBs consist of overlapping dislocation cores and display
²⁵² a high degree of miscoordination that is uniformly distributed along the GB area [25]. Hence,
²⁵³ it can be concluded from the figure that virtually all of the GBs in the supercell are high-angle
²⁵⁴ GBs which are visualized as continuous uninterrupted yellow lines. This also applies to all
²⁵⁵ the supercells employed in this work. Networks of GB dislocations have also been observed
²⁵⁶ along the GBs using the DXA in OVITO. These GB dislocations are not preferentially
²⁵⁷ aligned with any slip plane, are essentially immobile, and do not give rise to any dislocation-
²⁵⁸ dominated deformation that would interfere with diffusional creep. Additionally, sustainable
²⁵⁹ plastic deformation via the dislocation–nucleation mechanism is not possible because, e.g.,
²⁶⁰ the stress required to activate a Frank-Read source (a principal mechanism to sustain plastic
²⁶¹ deformation via dislocation multiplication [47]) increases inversely with decreasing grain size
²⁶² ($\sigma \sim 1/d$), and the size of a Frank-Read source cannot exceed the grain size [21, 48]. Thus,
²⁶³ our nanometer-sized grains are too small to accommodate a Frank–Read source that can
²⁶⁴ be activated by typical stresses. It has also been visually confirmed that the microstructure
²⁶⁵ does not undergo any micro-cracking, grain growth, GB sliding, or dislocation activity within
²⁶⁶ grain interiors during the time scale of the simulation.

²⁶⁷ Plots from the Coble creep simulations are shown in Fig. 2. An example of the strain
²⁶⁸ variation with time is shown in Fig. 2a. After the instantaneous elastic strain, a transient
²⁶⁹ strain stage is observed in which the strain rate decreases with time until it attains its
²⁷⁰ steady-state value. Temperatures and stresses were chosen to maintain steady-state creep
²⁷¹ throughout the simulation while simultaneously ensuring a sufficient signal-to-noise ratio in
²⁷² the strain response. The strain rate is calculated using a linear fit to the final 3 ns of the strain
²⁷³ versus time curve where steady-state creep is reached. The data was analyzed to parameterize
²⁷⁴ Eq. (4). To calculate the activation energy of creep, the Arrhenius plots of the strain rate
²⁷⁵ versus inverse temperature (e.g., Fig. 2b) have been fitted and an average value over all
²⁷⁶ grain sizes and stresses calculated. As shown in Table 1, the calculated activation energy is
²⁷⁷ $Q = 1.79 \pm 0.33$ eV, which is smaller than the activation energy of the Hayes correlation for
²⁷⁸ thermal creep in UN (Eq. (1), $Q = 3.39$ eV [5]), which assumes a dislocation mechanism,

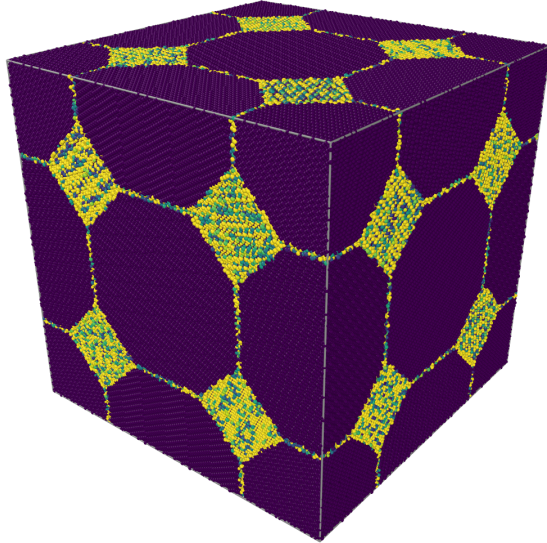


Figure 1: (Color online) UN polycrystalline supercell after energy minimization has been minimized at 0 K with a relative energy tolerance of 10^{-9} . To visualize the GB structure, atoms have been colored in OVITO according to their centrosymmetry parameter (CSP), where dark purple atoms have low CSP and yellow atoms have high CSP. For better visibility, the maximum CSP has been set to 20 \AA^2 .

and closer to the activation energy for GB diffusion in UN assumed by Konovalov *et al.* (i.e., $Q = 2.65 \text{ eV}$) [12]. This indicates that Coble creep can be a competitive mechanism to dislocation creep in UN. **It should be noted, however, that the large uncertainty in the activation energy can lead to more than an order of magnitude uncertainty in the predicted creep rate.**

Table 1: Coble creep parameters estimated from fitting the simulation results of the diffusional creep of UN. Uncertainties represent one standard deviation.

Activation energy, Q [eV]	Stress exponent, n	Grain size exponent, q
1.79 ± 0.33	1.35 ± 0.22	3.58 ± 0.87

To determine the dependence of the creep strain rate on the applied stress for each grain size and temperature, log-log plots of strain rate versus stress (Fig. 2c) have been fitted and the averaged value is shown in Table 1. A strain exponent $n = 1.35 \pm 0.22$ indicates that the stress dependence is nearly linear, which is characteristic of diffusional creep, and which agrees with the stress exponent found by Rogozkin *et al.* [9]. Following the same procedure for the stress exponent, the grain size exponent has been determined (Fig. 2d) for each applied stress and temperature, and the final averaged value is also shown in Table 1. It can be seen that the average grain size exponent $q = 3.58 \pm 0.87$ is very close to the grain size dependence of Coble creep ($q = 3$), but with relatively high uncertainty ($\sim 24\%$). Uncertainties of the fitting parameters in Table 1 are estimated by dividing the standard deviations by the mean values. It should be emphasized that only a subset of the data is shown in Figure 2, but the entire data set for all stresses, temperatures, and grain size are utilized in the determination of the average values in Table 1.

To confirm that the deformation mechanism is homogeneous (i.e., the total deformation of the supercell is proportional to the deformation of the individual grains), we visually con-

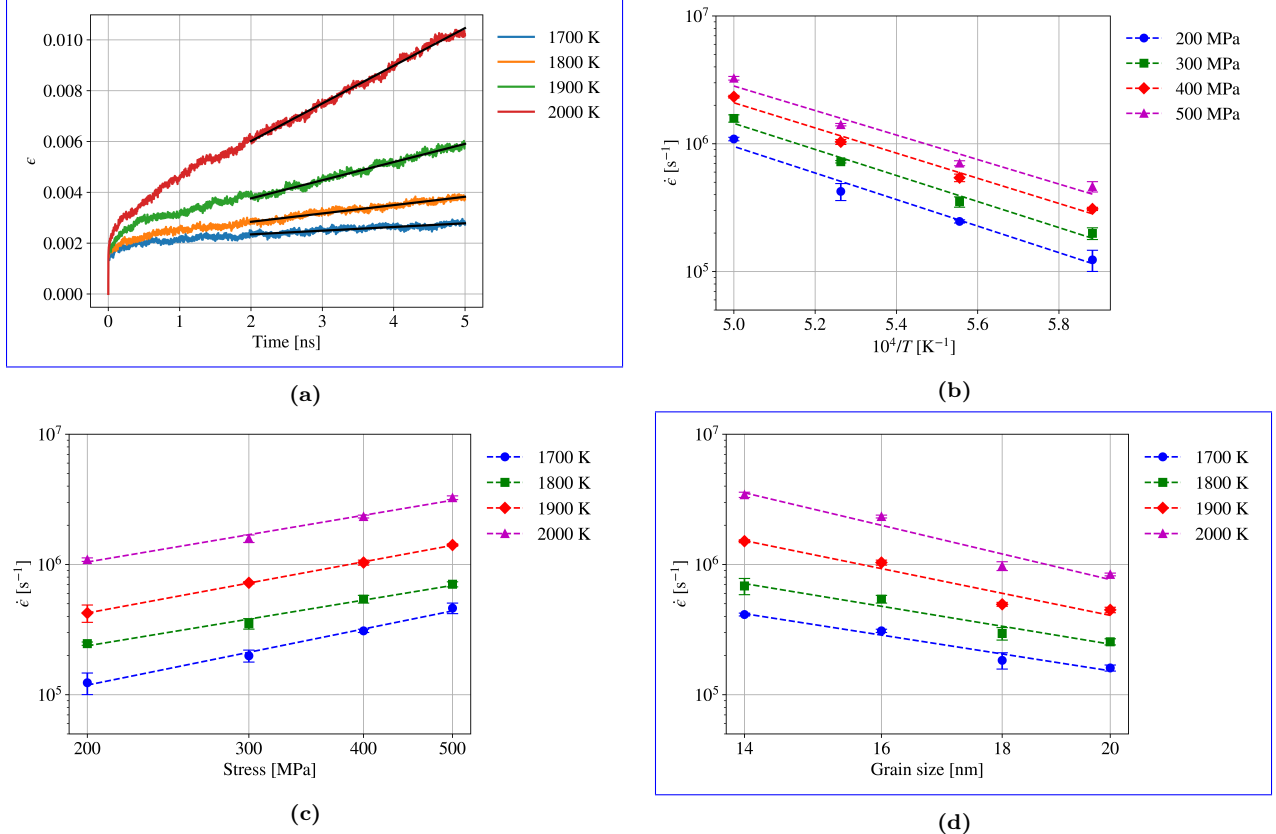


Figure 2: (Color online) (a) Variation of creep strain with time for a supercell with a grain size of 14 nm under constant stress of 200 MPa. (b) Semi-log plot of the variation of creep rate with inverse temperature for a supercell with a grain size of 16 nm. (c) Log-log plot of the variation of creep rate with stress for a supercell with a grain size of 16 nm. (d) Log-log plot of the variation of creep rate with grain size for supercells under constant stress of 400 MPa. In all figures, solid black lines correspond to the curve fits, and error bars correspond to one standard deviation.

298 firmed that the positions of the centers of mass of the grains, normalized by the instantaneous
 299 lengths of the cubic simulation box, did not move during the time scale of the simulation.
 300 Additionally, using the “displacement vectors” modifier in OVITO [33] it was confirmed that
 301 only atoms along the GBs undergo motion during the time scale of the simulations. That
 302 is, only Coble creep is observed in our simulations and Nabarro-Herring creep is essentially
 303 absent at the considered temperatures and time scale.

304 3.2. Parameter-based Coble creep model

305 Following the methodology of Cooper *et al.* [26] for $[..^{12}\text{U}_3\text{Si}_2]$ and Galvin *et al.* [..¹³
 306 [24] for UO_2 , we also construct a parameter-based Coble creep model. In this approach, the
 307 parameters of the Coble creep formula (Eq. (5)) are calculated independently.

¹²removed: U_3Si_2

¹³removed: [23] for UO_2

308 3.2.1. GB diffusivity

309 In ionic compounds like UN, the diffusional process requires ambipolar coupling to avoid
 310 compound decomposition [49]. This means that U and N atoms must diffuse in stoichiometric
 311 ratios with an effective diffusivity that is limited by the diffusivity of the slower species, i.e.,
 312 uranium, along its fastest path. The total effective diffusivity is calculated based on Gordon's
 313 formula [49] for ambipolar diffusion in an ionic solid $A_\alpha B_\beta$ (For UN, $\alpha = \beta = 1$):

$$D_{\text{eff}} = \frac{(\alpha + \beta)D_A D_B}{\beta D_A + \alpha D_B} \quad (7)$$

314 Eq. (7) differs from the usual formula for effective D by including the extra term $(\alpha + \beta)$,
 315 which appears because Gordon's formulation is based on the molecular volume of $A_\alpha B_\beta$
 316 whereas the traditional Coble creep formula (Eq. (5)) includes the average atomic volume
 317 [22, 50]. Because we are dealing with polycrystals, it is difficult to exclusively track the atomic
 318 movement within the GBs to determine the GB diffusivity. Instead, we track the movement
 319 of all atoms within the polycrystals. In this picture, the total diffusivity of either U or N
 320 atoms has both bulk and GB components. According to the Hart formulation [51, 52], the
 321 total diffusivity in a polycrystal can be divided between bulk and GB components according
 322 to:

$$D = cD_{\text{GB}} + (1 - c)D_b, \quad (8)$$

323 where c is the fraction of atoms that belong to the GBs (c will be defined quantitatively
 324 later in Section 3.2.2), D_{GB} is the GB diffusivity, and D_b is the bulk diffusivity. Thus, with
 325 the knowledge of the total diffusivity in the polycrystals and the bulk diffusivity, the GB
 326 diffusivity can be readily estimated.

327 To calculate the bulk diffusivities of U and N atoms, an unbound Schottky pair is ran-
 328 domly introduced within a $50 \times 50 \times 50$ UN supercell which is then equilibrated at temper-
 329 atures of 1700–2000 K and zero pressure under the *NPT* ensemble for 100 ps [53]. After
 330 equilibration, the mean squared displacements (MSD) of both species are averaged every
 331 1 ps for a total simulation time of 5 ns. The results are shown in Fig. 3a. It is apparent
 332 that the U atoms do not diffuse within bulk UN and only undergo vibrational motion in
 333 their positions. N atoms start to show non-zero diffusivity only at 2000 K and only vibrate
 334 around their equilibrium positions at lower temperatures. According to the Einstein relation,
 335 $\text{MSD} = 6Dt$ in the limit of an infinite time. Fitting the MSD curve for N atoms at 2000
 336 K over the final 3 ns gives $D_b^N = 5.91 \times 10^{-11} \text{ cm}^2/\text{s}$. This diffusivity value is negligible
 337 compared to the GB diffusivities of either U or N atoms (Fig. 3b, which will be described
 338 later in this subsection). Because U atoms do not undergo any measurable diffusivity, we
 339 can conclude that bulk diffusivity is essentially non-existent and all the atomic movement in
 340 the polycrystals can be solely attributed to GB diffusion.

341 The motion of all atoms in stress-free polycrystals with a grain size of 20 nm has been
 342 tracked. The polycrystal is equilibrated at the target temperature and zero pressure within
 343 the *NPT* ensemble for 50 ps. Then, the MSD of all atoms of both types is averaged every 1
 344 ps for a total averaging time of 5 ns. It was shown earlier that bulk diffusion is absent and
 345 all the atomic movement is attributed to diffusion along the GBs. Diffusion in the direction
 346 perpendicular to a GB is usually much smaller than the other two directions spanned by
 347 the GB, and GB diffusion is treated as a two-dimensional (2D) phenomenon [52]. Thus, we

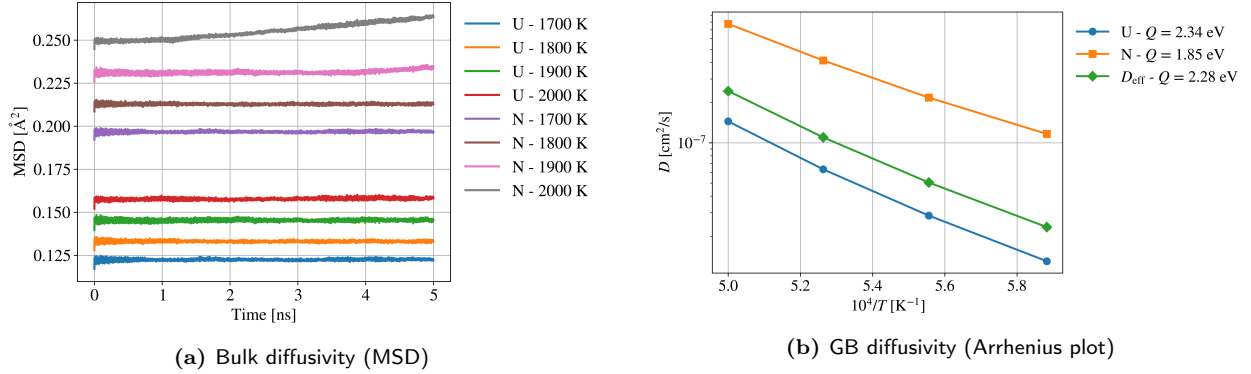


Figure 3: (Color online) (a) Mean squared displacements (MSD) of U and N atoms within bulk UN at different temperatures. A fit of the MSD curve for N atoms at 2000 K over the final 3 ns gives $D = 5.91 \times 10^{-11} \text{ cm}^2/\text{s}$. (b) Arrhenius plot of the GB diffusivity of U and N atoms, as well as the effective GB diffusivity. Note that the standard deviation of Q_U is $\pm 0.03 \text{ eV}$, and that of Q_N is $\pm 0.02 \text{ eV}$.

348 calculate the GB diffusivity of each atomic species by a linear fit of the MSD of that species
 349 over the last 3 ns to the 2D Einstein relation:

$$D_{\text{GB}}^{\text{U,N}} = \frac{1}{c} \frac{\text{MSD}^{\text{U,N}}}{4t}. \quad (9)$$

350
 351 The results of such calculations are shown in Fig. 3b. The calculation of the variable c
 352 for each temperature and grain size will be shown later. After getting the GB diffusivities of
 353 U and N atoms, the effective diffusivity is calculated based on Gordon's formula (Eq. (7)).
 354 The effective activation energy of GB diffusion is $Q = 2.28 \pm 0.09 \text{ eV}$ and the prefactor is
 355 $D_0 = 0.130 \pm 0.075 \text{ cm}^2/\text{s}$ (which has the typical order of magnitude). It can be seen that
 356 the activation energy of GB diffusion in stress-free polycrystals ($Q_{\text{eff}} = 2.28 \text{ eV}$) is closer
 357 to the assumed activation energy of GB diffusion in UN ($Q_{\text{GB}} = 2.65 \text{ eV}$ [12]) than the
 358 fitted activation energy of Coble creep simulation ($Q = 1.79 \text{ eV}$). Additionally, we repeated
 359 the GB diffusion calculation for grains with sizes of 14–18 nm and found that the standard
 360 deviation of Q_U is $\pm 0.03 \text{ eV}$, and that of Q_N is $\pm 0.02 \text{ eV}$. Compared to this, the fitted
 361 activation energy of Coble creep has a larger uncertainty of $\pm 0.33 \text{ eV}$. This discrepancy can
 362 be attributed to the stress effect on GB diffusion. In general, GB diffusivity increases with
 363 the applied stress [25], which might be manifested by a reduction in the activation energy.
 364 A reduction in the activation energy stems from an increase of the GB diffusivity at the
 365 higher temperatures for which the stress effect on the GB diffusivity is more pronounced. It
 366 is also observed that the activation energy for the effective diffusivity is nearly dominated by
 367 that of U atoms, which confirms the assertion that the GB diffusion of the slowest-moving
 368 species, i.e., U atoms, is rate-limiting for Coble creep.

369 3.2.2. Grain-boundary width

370 Next, we closely analyze the GB width. At first, we need to differentiate between two
 371 concepts of GB width in high-purity materials [46, 54]: (a) diffusional GB width, δ_d , which
 372 corresponds to the width within which atoms diffuse, and (b) structural GB width, δ_s , which
 373 corresponds to the width within which miscoordinated atoms exist, whether they diffuse or

374 not. Kebinski *et al.* [46] found in their atomistic simulations that δ_d is thermally activated
 375 and shows an Arrhenius dependence on temperature. However, their analysis was based on
 376 bicrystals, which usually contain symmetric tilt GBs and are not necessarily representative
 377 of realistic microstructures. Additionally, the analysis was conducted at temperatures near
 378 the melting point, which are not usually accessible in GB diffusion experiments due to the
 379 simultaneous contribution of bulk diffusion at these high temperatures. Thus, their results
 380 could not be experimentally verified. On the other hand, Prokoshkina *et al.* [54] conducted
 381 an extensive analysis of the measured GB widths of various metals and compounds and found
 382 that the GB widths measured in GB diffusion measurements do not show any dependence
 383 on temperature or grain size. The purpose of this section is to resolve this apparent conflict
 384 between atomistic simulations and experiments and provide a consistent definition for GB
 385 width that can be extracted from atomistic simulations and agrees with the experimental
 386 data. We begin by using our GB diffusivity data to extend the analysis from Kebinski *et al.*
 387 to polycrystals of uniform size and shape and temperatures relatively far from the melting
 388 point.

389 The diffusion flux at the GB (in m^3/s) is a product of the GB diffusivity and diffusional
 390 GB width: $D_{\text{GB}}\delta_d$, and can be expressed as follows:

$$D_{\text{GB}}\delta_d = \lim_{t \rightarrow \infty} \frac{\Omega}{A} \frac{\sum_{i=1}^{N_{\text{GB}}} |\Delta \mathbf{r}_i(t)|^2}{6t} \approx \lim_{t \rightarrow \infty} \frac{\text{MSD}_{\text{GB}}(T)}{6t} \frac{\Omega N_{\text{GB}}(T)}{A} \quad (10)$$

391 where both the MSD of GB atoms, MSD_{GB} , and the number of atoms *diffusing* within the
 392 GB, N_{GB} , are functions of temperature. In [Appendix A](#), we derive the following formula
 393 for the diffusional GB width of polycrystals:

$$\delta_d = \eta c V^{1/3} \quad (11)$$

394 where V is the volume of a space-filling grain and c is defined as the fraction of atoms that
 395 have undergone non-affine displacements of at least the nearest-neighbor distance in the
 396 limit of infinite simulation time. For UN, the nearest-neighbor distance is $0.5a$, where a is
 397 the lattice parameter. c can be estimated using the displacement-vectors (DV) modifier in
 398 OVITO [33] applied to snapshots of the polycrystal. η is a shape factor that depends on the
 399 grain shape. For truncated-octahedral grains, $\eta = 0.376$ ([Eq. \(A.5\)](#)). Note that, unlike the
 400 calculation of the GB diffusivity which is based on averages taken during the MD simulation,
 401 the estimation of the GB width is a post-processing step.

402 Although [Eq. \(11\)](#) is derived for grains of uniform size and shape, it is principally applic-
 403 able to grains of random sizes and shapes provided that the average *grain volume* is treated
 404 as the volume of a truncated octahedral grain and the grain size distribution is relatively
 405 narrow. In this case, [Eq. \(11\)](#) can be readily applied to estimate δ_d for any polycrystal
 406 using $\eta = 0.376$. The advantage of this method is that it enables us to determine δ_d for a
 407 microstructure that contains realistic grain features like triple lines and quadruple junctions.
 408 In contrast to other methods based on bicrystal simulations, our proposed method simulta-
 409 neously samples many GBs with various misorientations and gives an effective value for δ_d
 410 averaged over all of them.

411 This analysis is implicitly based on two assumptions. First, in the limit of a very long
 412 time, the number of GB atoms that have moved by at least the nearest-neighbor distance

will saturate to a value determined by the temperature. This was assumed by Kebinski *et al.* [46] but never proved. To demonstrate that this is indeed the case, we use OVITO's DV modifier to track the number of diffusing atoms in a stress-free 20-nm supercell. To probe the effect of the stress and the grain size on the diffusional GB width, we conduct the same analysis for the 20-nm supercell under stresses of 400 MPa and 500 MPa and the 18-nm supercell under a stress of 500 MPa. In all cases, the number of diffusing atoms is fitted to a saturation function of the form:

$$N_{\text{GB}} = N_0 (1 - e^{-\lambda t}) + C \quad (12)$$

In the limit of infinite time, the exponential [...] approaches zero, and $N_{\text{GB}} = N_0 + C$. Note that N_{GB} represents the asymptotic (saturation) number of atoms participating in Coble creep once steady-state grain boundary diffusion is fully established. The result of the fitting for the 20-nm supercell under no stress is shown in Fig. 4a, which demonstrates that N_{GB} perfectly follows a saturation function, and that the saturated value of N_{GB} increases with increasing temperature. Similar trends have been observed for the other tracked supercells. The saturated values of $N_{\text{GB}} = N_0 + C$ are then fitted to an Arrhenius-type function. The results of such fitting for the tracked supercells are shown in Fig. 4b, which shows that the diffusional GB width perfectly follows an Arrhenius behavior that is independent of supercell grain size and applied stress. The activation energy for all tracked supercells is 0.74 ± 0.01 eV for the 20-nm supercell at all stress values and 0.82 eV for the 18-nm supercell. While the effect of grain size on Q_δ is quite small, the effect of stress is essentially non-existent. Based on their bicrystal calculation, Kebinski *et al.* [46] estimated the activation energy of the GB width in Pd to be 0.22 eV.

While these results corroborate the computational findings of Kebinski *et al.*, this Arrhenius dependence still contradicts the experimental observations that the measured GB width is independent of temperature. This leads to our second assumption: the GB width in the Coble creep formula corresponds to a temperature-independent (effective) GB width, which is calculated by extrapolating the diffusional GB width to the melting point where all miscoordinated atoms are assumed to have undergone diffusion. Extrapolating the Arrhenius curves in Fig. 4b to 2700 K (the melting point as predicted by the Tseplyaev potential [29]), the effective GB width is found to be $\delta = 2.69 \pm 0.08$ nm. This GB width should correspond to the diffusion of all the GB atoms and is the one we use in the parameter-based Coble creep formulation. We show later that this value of the GB width provides an excellent prediction of the prefactor in the phenomenological Coble creep formula, which supports our second assumption.

Lastly, we need to discuss the c parameter in Eq. (11), which is used in Eq. (9) to estimate the GB diffusivity. In analogy with the two definitions of the GB width, there are two definitions of the c parameter: (a) the fraction of atoms that diffuse within the GBs, and (b) the fraction of miscoordinated atoms existing within the GBs, whether they diffuse or not. A third definition [12] is to estimate c as the volume fraction of the GBs based on the formula:

$$c = \frac{3\delta}{d} \quad (13)$$

¹⁴removed: dies out

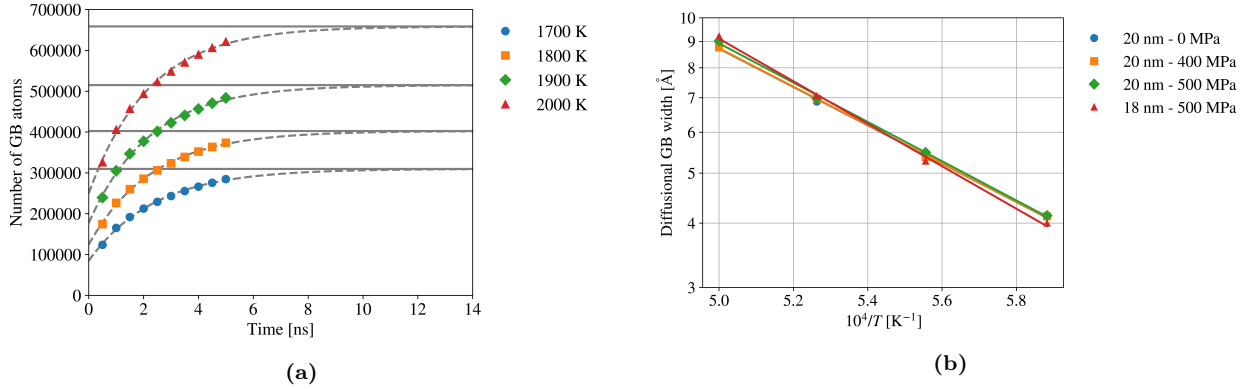


Figure 4: (Color online) (a) The variation of the number of GB atoms, N_{GB} , with time for the polycrystal with a grain size of 20 nm under no stress. In the limit of [\dots^{15}] infinite time, N_{GB} reaches a saturation value that increases with increasing temperature. (b) Arrhenius plot of the diffusional GB width for the tracked supercells. The activation energy of δ_d ranged between 0.74 and 0.82 eV.

452 where δ is the GB width, and d is the grain diameter. The same procedure of calculating
 453 the GB width is used to extract the c parameter of the 20-nm polycrystal to calculate the
 454 GB diffusivity in [Section 3.2.1](#). Note that the *saturated* number of GB atoms is linearly
 455 proportional to the diffusional GB width ([Eq. \(A.1\)](#)), and, thus, both follow an Arrhenius
 456 behavior with the same activation energy. Like the GB width, we extrapolate the Arrhenius
 457 plot of the saturated number of GB atoms up to the melting temperature to extract the
 458 number of miscoordinated atoms. This number is then divided by the total number of atoms
 459 in the supercell to get c . Based on this procedure, $c = 0.44 \pm 0.01$ for the stress-free 20-nm
 460 polycrystal. It should be noted that if we used $\delta = 2.69$ nm, and $d = 20$ nm in [Eq. \(13\)](#),
 461 we get $c = 0.40$. That is, the definitions of c based on the volume fraction or the atomic
 462 fraction give very close results and can be used interchangeably. For macroscopic systems
 463 with d in the μm -range, $c \sim 10^{-3}$. In effect, c penalizes the nm-sized structures for having
 464 grains with a large surface-to-volume ratio.

465 3.2.3. Vacancy volume

466 The remaining unknown parameter in the Coble creep model ([Eq. \(5\)](#)) is the vacancy
 467 volume. To calculate the vacancy volume in UN, we construct $6 \times 6 \times 6$ perfect supercells
 468 and calculate the volume of the minimized structure at 0 K. Then, we separately delete U
 469 and N atoms from the center of the supercell, minimize the energy of the defective structure,
 470 and finally calculate the vacancy volume as the volume difference between the pristine and
 471 defective crystals. All structures have been minimized with a relative energy tolerance of
 472 10^{-9} . The result of such calculations is presented in [Table 2](#), where the atomic volume is also
 473 given for reference. We use the values of the Tspelyaev potential, but those calculated by
 474 the Kocevski potential are also shown for comparison. It can be observed that the Kocevski
 475 potential predicts a positive volume for the N vacancy, which is unphysical. The reason for
 476 this is that upon removing the N atom, there is no longer a screening/shielding between the
 477 U atoms, which repel each other and lead to [\dots^{16}] an increase in the volume of the supercell

¹⁶removed: increasing

478 with the vacancy. This is due to the inability of the Kocevski potential to model metallic
 479 U. From Table 2, we take the absolute value of V_U as the vacancy volume, i.e., $\Omega = 4.963$
 480 \AA^3 . [..¹⁷] The vacancy volume is nearly one-third of the atomic volume (13.909\AA^3), indicating
 481 that the commonly used approximation of equating Ω to atomic volume [18] is not accurate for
 482 UN. The discrepancy arises from the local lattice relaxation and volume shrinkage induced by the
 483 formation of a vacancy, highlighting the importance of calculating Ω explicitly. To conclude, all
 484 the values for the parameter-based Coble creep model are summarized in [..¹⁸] Table 3.

Table 2: Vacancy and atomic volumes (in \AA^3) as predicted by the Tseplyaev and Kocevski potentials. $\Omega(\text{atom})$ is the average volume of a single atom.

	$\Omega(V_U)$	$\Omega(V_N)$	$\Omega(\text{atom})$
Tseplyaev potential	-4.963	-0.227	13.909
Kocevski potential	-1.990	4.350	14.685

485 As a sanity check of our calculated parameters, according to the Mukherjee-Bird-Dorn
 486 phenomenological model of Coble creep [34], the product $A_C\Omega\delta$ should numerically equal
 487 $50b^4$ where b is the Burgers vector. With $A_C = [..¹⁹] 46.347$, we find that $A_C\Omega\delta = 6195$
 488 \AA^4 , whereas $50b^4 = 6691 \text{\AA}^4$, with a difference of only [..²⁰] 7.52%. This also supports our
 489 method in calculating the GB width and its associated assumptions. In other words, although
 490 atomistic simulations reveal a temperature-dependent diffusional GB width, this behavior is not
 491 attributed to the limited timescales accessible to MD. Rather, our analysis shows that the number
 492 of diffusing atoms within GBs saturates with time and increases with temperature, resulting in
 493 an Arrhenius dependence of the diffusional GB width. In contrast, experimental GB widths
 494 reflect a long-time effective value that is typically temperature-independent. Additionally, the
 495 experimentally measured GB width can vary depending on the measurement technique. High-
 496 resolution transmission electron microscopy (HRTEM) yields the structural GB width, which is
 497 precise but not directly relevant to diffusional creep studies [54]. In contrast, GB widths inferred
 498 from diffusion data are more relevant but are less reliable due to uncertainties associated with
 499 data fitting [54]. To reconcile simulation and experimental perspectives, we extrapolated the
 500 temperature-dependent diffusional GB width to the melting point and defined this extrapolated
 501 value as the effective GB width to be used in the Coble creep formulation. This value (2.69
 502 nm) reproduces the expected prefactor in the Coble creep equation and provides a consistent
 503 physical basis for incorporating MD-based GB width estimates into mesoscale models. It should
 504 be mentioned that the proposed method for estimating the effective GB width is general and
 505 transferable, as it relies solely on atomistic trajectories and makes no assumptions about the
 506 material's chemistry, crystal structure, or defect energetics.

¹⁷removed: All the

¹⁸removed: in

¹⁹removed: 46.374

²⁰removed: 7.42

Table 3: Values for the parameter-based Coble creep model.

Coble prefactor, A_C	46.347
Vacancy volume, Ω	$4.963 \times 10^{-30} \text{ m}^3$
Effective GB width, δ	$2.69 \times 10^{-9} \text{ m}$
GB diffusivity prefactor, D_0	$1.30 \times 10^{-5} \text{ m}^2/\text{s}$
GB diffusivity activation energy, Q	2.28 eV

507 *3.2.4. Comparison of Creep Predictions*

508 We compare the simulation and parameter-based models of Coble creep in UN developed
 509 in this work to Coble creep in UO_2 as calculated by Galvin *et al.* [24]. The
 510 prefactor in the simulation model was calculated by utilizing the values in Table 1 [23]
 511 *within Eq. (4)*. The prefactor was found to have a numerical value of $A = 3.424 \times 10^{-26}$.
 512 For both fuels, a stress of 15 MPa, and a grain size of 10 μm were assumed. The result
 513 of such a comparison is shown in Fig. 5. It can be seen that the two models of Coble
 514 creep in UN agree to less than an order of magnitude, especially at lower temperatures.
 515 Additionally, irrespective of the creep model, the Coble creep rate of UN is approximately
 516 one order of magnitude larger than that of UO_2 . It is also an order of magnitude larger
 517 than the Hayes *et al.* correlation for dislocation creep in UN. Although a stress of 15 MPa
 518 is outside the stress range of the Hayes creep correlation (i.e., [25] 20–34 MPa), it is not
 519 very far from the range's lower limit, and we assume it can at least provide an estimate
 520 of the dislocation creep rate for stresses slightly smaller or larger than the reported stress
 521 applicability range. This comparison shows that Coble creep in UN can be more dominant
 522 than (or is at least competitive [26] *with*) dislocation creep. This agrees with the qualitative
 523 analysis by Konovalov *et al.* [12]. It should be mentioned that Galvin *et al.* [27] [24] used
 524 a Coble creep prefactor $A_C = 42\pi$ for their UO_2 Coble creep formula, whereas in this
 525 work [29], we use $A_C = 46.347$. However, the difference between the two values is only a
 526 factor of 3, which would have little effect on the results in Fig. 5.

527 Merely comparing the properties of different fuel systems within a temperature range
 528 might not accurately represent how the fuel systems behave in reactor conditions. More
 529 appropriately, we should compare fuel behaviors at representative center-line temperatures
 530 [55]. Considering the high thermal conductivity of UN, it is expected that the center-line
 531 temperatures and temperature gradients of UN fuel rods are much lower than [34] *those of*
 532 UO_2 fuel rods under the same conditions. For example, based on their finite-element analysis
 533 of the thermal-mechanical behavior of several advanced fuel-cladding combinations, Zeng *et*

²¹removed: UO_2

²²removed: [23]

²³removed: in

²⁴removed: UO_2

²⁵removed: 20–34

²⁶removed: to

²⁷removed: [23]

²⁸removed: UO_2

²⁹removed: we use $A_C = 46.374$

³⁴removed: that of UO_2

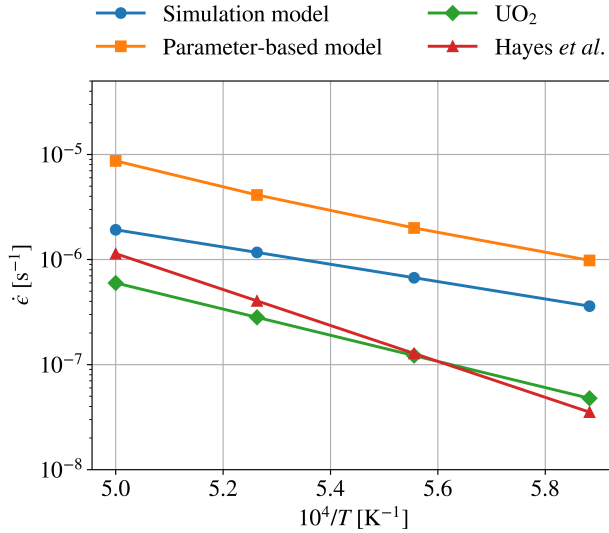


Figure 5: Comparison between the simulation and parameter-based models of Coble creep in UN developed in this work to Coble creep in $[..^{30}]UO_2$ in the temperature range 1700–2000 K for a stress of 15 MPa, and a grain size of 10 μm . The $[..^{31}]UO_2$ data is taken from $[..^{32}][24]$. $[..^{33}]$ The Hayes *et al.* [5] correlation for dislocation creep is also presented for comparison.

534 *al.* [56] have estimated the early-life centerline temperature of the $[..^{35}]UO_2$ -FeCrAl fuel
 535 system to be about 1300 K, whereas it is only about 900 K for the UN-FeCrAl fuel system.
 536 Thus, under the same early-life reactor conditions, the creep of UN is expected to be less
 537 pronounced than that of $[..^{36}]UO_2$. The effect of irradiation on this comparison, however,
 538 requires a separate study.

539 4. Discussion

540 Parameters in Table 1 calculated from the fitting of the diffusional creep simulation have
 541 about 16-24% uncertainty, which is reasonable considering that each strain rate is an average
 542 over three unique simulations. The uncertainty can be reduced by simulating for longer times
 543 or averaging over more runs. However, this is computationally expensive for the supercells
 544 at hand, whose number of atoms ranges between 1,547,344 atoms for the 14-nm polycrystal
 545 [$..^{37}$] and 4,537,943 atoms for the 20-nm polycrystal. Due to the much lower computational
 546 cost and smaller uncertainties, the parameter-based Coble creep model is recommended for
 547 use [$..^{38}$] in the determination of a Coble creep rate.

548 While the simulations presented in this work utilize nanometer-scale polycrystals (14–20 nm)
 549 to achieve sufficient creep strain within accessible MD time scales, the fundamental deformation
 550 mechanism, namely, diffusional creep mediated by GB diffusion, is governed by well-established
 551 scaling laws. The Coble creep model inherently accounts for grain size effects, combined with

³⁵removed: UO_2

³⁶removed: UO_2

³⁷removed: ,

³⁸removed: for

552 the several hundred MPa stresses, through its σ/d^3 dependence, enabling extrapolation of MD-
 553 obtained parameters to realistic microstructural scales (on the order of micrometers) and typical
 554 creep stresses (tens of MPa).

555 An important aspect of this work is that we investigated the temperature dependence
 556 of the diffusional GB width and proposed a consistent method to calculate an effective GB
 557 width for the Coble creep formula. We found that the diffusional GB width in UN follows
 558 an Arrhenius behavior with an activation energy of about $Q_\delta = 0.74\text{--}0.82$ eV. Kebinski
 559 *et al.* [46] assumed that the activation energy of GB diffusion ($Q = 2.28$ eV in our case)
 560 can be expressed as $Q = Q_\delta + Q_{\text{amorph}}$, where Q_{amorph} is the activation energy for diffusion
 561 in the amorphous structure of the GB. Based on this assumption, Q_{amorph} should be 1.47–
 562 1.55 eV. For this assumption to be verified experimentally, amorphous diffusion coefficients
 563 need to be measured for UN. However, it was never reported that UN amorphizes under
 564 irradiation. However, this does not affect our estimated GB width which nearly perfectly
 565 predicts the prefactor of the Coble creep formula, i.e., Eq. (5). Our two Coble creep models
 566 closely agree, especially at lower temperatures. However, considering that the parameter-
 567 based model generally exhibits smaller uncertainties in its calculated parameters, is much
 568 less computationally expensive, and can be more easily extended to a larger temperature
 569 range, we recommend its use in fuel performance codes. For ease of access, the complete
 570 Coble creep rate equation is provided here:

$$\dot{\epsilon} = 582610.427 \frac{\sigma}{Td^3} \exp\left(-\frac{2.28 \text{ eV}}{k_B T}\right), \quad (14)$$

571 where σ is the stress in MPa, T is the temperature in K, d is the average grain size in μm ,
 572 and $\dot{\epsilon}$ is the creep rate in s^{-1} .

573 The activation energy of Coble creep in UN is about 1 eV smaller than that of the
 574 dislocation-mediated creep estimated by Hayes *et al.* [5] and is very close to the activation
 575 energy of GB diffusion in UN assumed by Konovalov *et al.* [12]. This implies that there is
 576 a surface in the σ, d, T -space that separates regions in which Coble creep is dominant from
 577 other regions where dislocation creep is dominant. To examine this idea in some detail, we use
 578 Eqs. (1) and (14) (our Coble creep correlation and the Hayes dislocation creep correlation)
 579 to construct deformation mechanism maps for UN to identify regions where Coble creep is
 580 dominant and others where dislocation creep is dominant. Deformation mechanism maps
 581 that examine the dominant creep mechanisms for different grain sizes and stresses at $T =$
 582 1800 K and 2200 K are shown in Figs. 6a and 6b, respectively. As expected, as the grain size
 583 is increased, dislocation creep becomes more dominant. The red solid line in Figs. 6a and 6b
 584 refers to the grain size and stress range of the creep rate measurements by Fassler *et al.* [6],
 585 which had a stress exponent of about 4.7. The measurements are clearly in the dislocation
 586 creep region which explains the high stress exponent. It should be mentioned that Fassler
 587 *et al.* data were obtained at 1373–1623 K.

588 Interestingly, at $d = 10 \mu\text{m}$, the upper limit of the optimum UN grain sizes [14], and
 589 the stress range of 20–30 MPa, within which the Hayes correlation was fitted, Coble creep is
 590 more dominant than dislocation creep at 1800 K, and both are nearly equally present at 2200
 591 K. Thus, a contribution of both creep mechanisms will be observed with the contribution
 592 of the dislocation creep increasing with increasing temperature or increasing the grain size.
 593 Similar deformation mechanism maps for $d = 10$ and $20 \mu\text{m}$ are shown in Figs. 6c and 6d,

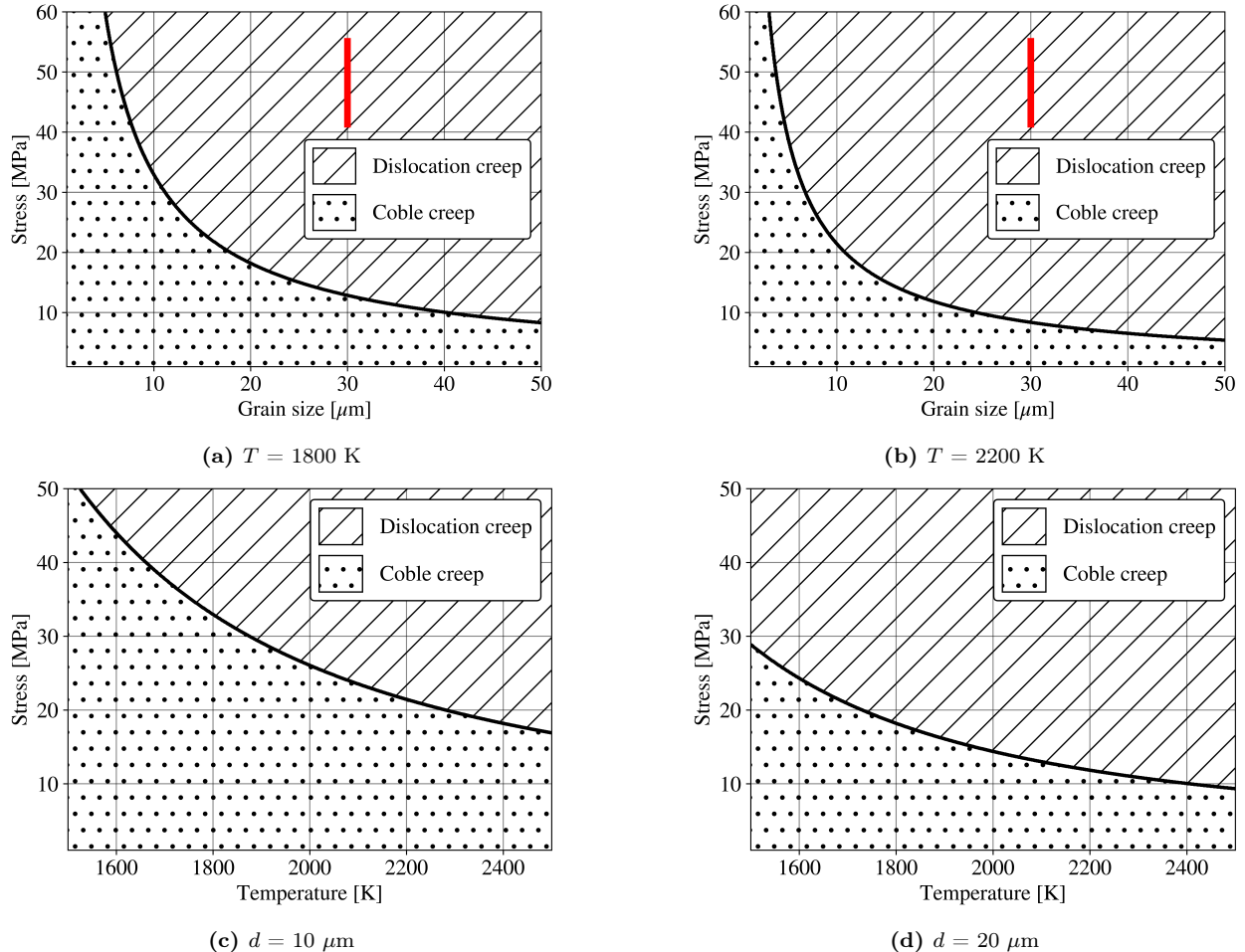


Figure 6: (Color online) Deformation mechanism maps of the dominant creep mechanism for different grain sizes and stresses at (a) $T = 1800$ K and (b) $T = 2200$ K. The red solid line in (a) and (b) refers to the grain size and stress range of the creep rate measurements by Fassler *et al.* [6]. Deformation mechanism maps of the dominant creep mechanism for different temperatures and stresses at (c) $d = 10 \mu\text{m}$ and (d) $d = 20 \mu\text{m}$.

respectively, for different temperatures and stresses. For a stress of 20 MPa and $d = 10 \mu\text{m}$, dislocation creep becomes apparent at about $T = 2200$ K, whereas for $d = 20 \mu\text{m}$, Coble creep is only present at temperatures below $T = 1700$ K, where the creep rate is small anyway. The most general thermal creep correlation for UN should be a sum of both contributions:

$$\dot{\epsilon}_{\text{tot}} = 582610.427 \frac{\sigma}{Td^3} \exp\left(-\frac{2.28 \text{ eV}}{k_B T}\right) + 2.054 \times 10^{-3} \sigma^{4.5} \exp\left(-\frac{3.39 \text{ eV}}{k_B T}\right), \quad (15)$$

where T is in K, σ is in MPa, and d is in μm . To test this final correlation, we compare it to the experimental data of Uchida and Ichikawa [8] in Fig. 7. For the grain size of 9 μm , the correlation gives an excellent prediction of the experimental creep rate. For the grain size of 15 μm , Eq. (15) underestimates the creep rate by at most an order of magnitude, which can be considered fair qualitative agreement taking into account that the 15- μm samples of Uchida and Ichikawa [8] experienced a significant hot-pressing effect.

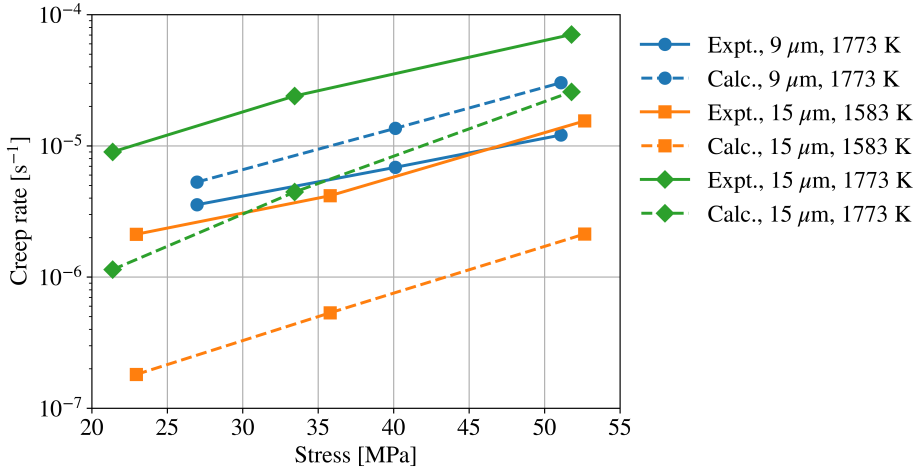


Figure 7: (Color online) Comparison of the experimental creep rate data of Uchida and Ichikawa [8] to that calculated using Eq. (15).

While the present work addresses thermally activated diffusional creep in pristine UN, irradiation is expected to significantly influence creep behavior under reactor-relevant conditions. In particular, irradiation-enhanced diffusion can markedly increase atomic transport rates and enable creep rates far exceeding those predicted from thermal diffusion alone [26]. Consequently, the results presented here should be interpreted as a lower bound on in-service creep behavior and motivate future studies that explicitly incorporate radiation damage.

5. Conclusions

In this study, we employed MD simulations to investigate specific aspects of the mechanical behavior of UN. The diffusional creep simulations were conducted using nanometer-sized polycrystals with realistic microstructural features. Results indicate that Nabarro-Herring creep is not active within the studied temperature range and time scale. Instead, Coble creep emerges as the dominant diffusional creep mechanism, exhibiting an activation energy of 2.28 eV. A method is introduced to compute the diffusional GB width and its temperature dependence in polycrystals. The diffusional GB width of UN is observed to follow an Arrhenius behavior with an activation energy of 0.74–0.82 eV. The value of the diffusional GB width at the melting point is estimated as 2.69 nm, which we treat as an effective GB width to be used in the Coble creep formula. This value shows an excellent prediction of the prefactor of the phenomenological Coble creep formula. The parameter-based model of Coble creep in UN agrees with the simulation model and shows less uncertainty at less computational cost. It is shown that the most general thermal creep correlation of UN is a sum of our Coble creep correlation and the Hayes *et al.* dislocation creep correlation.

626 **6. Acknowledgements**

627 The authors [..³⁹] thank Khadija Mahbuba and Mahmoud Hawary for the fruitful discussions
 628 and useful suggestions. This work is funded by [..⁴⁰] Westinghouse Electric Company.
 629 This research made use of the resources of the High-Performance Computing Center at
 630 Idaho National Laboratory, which is supported by the Office of Nuclear Energy of the U.S.
 631 Department of Energy and the Nuclear Science User Facilities under Contract No. DE-
 632 AC07-05ID14517. Mohamed AbdulHameed dedicates this work to Ayman AbdulRaheem.

633 **Appendix A. Derivation of the diffusional GB width formula**

634 An estimate of the diffusional GB width can be made based on the formula [46]:

$$\delta_d = \frac{N_{\text{GB}}\Omega}{A} \quad (\text{A.1})$$

635 where N_{GB} is the number of atoms existing within the GBs, Ω is the atomic volume, and
 636 A is the GB area. The number of GB atoms can be defined as $N_{\text{GB}} = cN$ [25] where c is
 637 defined as the fraction of atoms that have undergone non-affine displacements of at least one
 638 nearest-neighbor distance in the limit of infinite simulation time, and N is the total number
 639 of atoms in the supercell. The atomic volume is $\Omega = gV/N$, where g is the number of grains
 640 in the supercell (in our case, $g = 16$), and V is the grain volume. Because the grains are
 641 space-filling, the supercell volume $l_x l_y l_z = gV$. The GB area is $A = gS/2$, where S is the
 642 grain surface area, which for a truncated octahedron is given by [57]:

$$S = \left(6 + 12\sqrt{3}\right) l^2 \quad (\text{A.2})$$

643 where l is the truncated octahedron's edge length, which can be calculated from [57]:

$$l = \left(\frac{V}{8\sqrt{2}}\right)^{1/3} \quad (\text{A.3})$$

644 Thus, for the case of a supercell containing truncated-octahedral grains of uniform size and
 645 shape, the diffusional GB width is:

$$\delta_d = 2c \frac{V}{S} = \eta c V^{1/3} \quad (\text{A.4})$$

646 where η is a shape factor that depends on the grain shape. For truncated-octahedral grains:
 647

$$\eta = \frac{4 \times 2^{1/3}}{3 + 6\sqrt{3}} \approx 0.376. \quad (\text{A.5})$$

648 This derivation assumes that the grains are space-filling and of uniform shape and size. It is
 649 interesting to note in Eq. (A.4) that while the GB width, δ , depends on the grain volume-
 650 to-surface ratio, V/S , which increases with increasing the grain size, δ also depends on c ,
 651 which increases both with increasing the temperature and the grain surface-to-volume ratio.
 652 That is, this definition of the GB width takes into account both structural and diffusional
 653 aspects.

³⁹removed: would like to

⁴⁰removed: the

654 **References**

- 655 [1] C. Ekberg, D. R. Costa, M. Hedberg, M. Jolkkonen, Nitride fuel for Gen IV nuclear
656 power systems, *Journal of Radioanalytical and Nuclear Chemistry* 318 (2018) 1713–
657 1725. [doi:10.1007/s10967-018-6316-0](https://doi.org/10.1007/s10967-018-6316-0).
- 658 [2] J. Wallenius, Nitride fuels, *Comprehensive Nuclear Materials* 5 (2020) 88–101. [doi:10.1016/B978-0-12-803581-8.11694-7](https://doi.org/10.1016/B978-0-12-803581-8.11694-7).
- 660 [3] M. Uno, T. Nishi, M. Takano, Thermodynamic and thermophysical properties of
661 the actinide nitrides, *Comprehensive Nuclear Materials: Second Edition* (2020) 202–
662 231[doi:10.1016/B978-0-12-803581-8.11749-7](https://doi.org/10.1016/B978-0-12-803581-8.11749-7).
- 663 [4] D. Frazer, B. Maiorov, U. Carvajal-Nuñez, J. Evans, E. Kardoulaki, J. Dunwoody, T. A.
664 Saleh, J. T. White, High temperature mechanical properties of fluorite crystal structured
665 materials (CeO_2 , ThO_2 , and UO_2) and advanced accident tolerant fuels (U_3Si_2 , UN, and
666 UB_2), *Journal of Nuclear Materials* 554 (2021). [doi:10.1016/j.jnucmat.2021.153035](https://doi.org/10.1016/j.jnucmat.2021.153035).
- 667 [5] S. L. Hayes, J. K. Thomas, K. L. Peddicord, Material property correlations for uranium
668 mononitride II. mechanical properties, *Journal of Nuclear Materials* 171 (1990) 271–288.
- 669 [6] M. Fassler, F. Huegel, M. DeCrescente, The compressive creep of UC and UN, Tech.
670 Rep. PWAC-482, Pratt & Whitney Aircraft Co. (1965).
- 671 [7] R. Vandervoort, W. Barmore, C. Cline, Compressive creep of polycrystalline uranium
672 mononitride in nitrogen, *Transactions of the Metallurgical Society of AIME* 242 (1968)
673 1466–1467.
- 674 [8] M. Uchida, M. Ichikawa, Compressive creep of sintered UC-UN solid solutions, *Journal*
675 *of Nuclear Materials* 49 (1973). [doi:10.1016/0022-3115\(73\)90065-2](https://doi.org/10.1016/0022-3115(73)90065-2).
- 676 [9] B. D. Rogozkin, N. M. Stepenova, A. A. Proshkin, Mononitride fuel for fast reactors,
677 *Atomic Energy* 95 (2003). [doi:10.1023/B:ATEN.0000007886.86817.32](https://doi.org/10.1023/B:ATEN.0000007886.86817.32).
- 678 [10] M. Meyers, K. Chawla, *Mechanical Behavior of Materials*, 2nd Edition, Cambridge
679 University Press, 2009.
- 680 [11] E. A. Kotomin, Y. A. Mastrikov, S. N. Rashkeev, P. V. Uffelen, Implementing first
681 principles calculations of defect migration in a fuel performance code for UN simulations,
682 *Journal of Nuclear Materials* 393 (2009) 292–299. [doi:10.1016/j.jnucmat.2009.06.016](https://doi.org/10.1016/j.jnucmat.2009.06.016).
- 684 [12] I. I. Konovalov, B. A. Tarasov, E. M. Glagovsky, Structural-phase state and creep of
685 mixed nitride fuel, in: *IOP Conference Series: Materials Science and Engineering*, Vol.
686 130, 2016. [doi:10.1088/1757-899X/130/1/012030](https://doi.org/10.1088/1757-899X/130/1/012030).
- 687 [13] J. Adachi, K. Kurosaki, M. Uno, S. Yamanaka, M. Takano, M. Akabori, K. Minato, Me-
688 chanical properties at sub-microscale and macroscale of polycrystalline uranium monon-
689 itride, *Journal of Nuclear Materials* 384 (2009) 6–11. [doi:10.1016/j.jnucmat.2008.09.019](https://doi.org/10.1016/j.jnucmat.2008.09.019).

- 691 [14] K. D. Johnson, D. A. Lopes, Grain growth in uranium nitride prepared by spark plasma
692 sintering, Journal of Nuclear Materials 503 (2018). [doi:10.1016/j.jnucmat.2018.02.041](https://doi.org/10.1016/j.jnucmat.2018.02.041).
- 694 [15] K. Yang, E. Kardoulaki, D. Zhao, A. Broussard, K. Metzger, J. T. White, M. R. Sivack,
695 K. J. McClellan, E. J. Lahoda, J. Lian, Uranium nitride (UN) pellets with controllable
696 microstructure and phase - fabrication by spark plasma sintering and their thermal-
697 mechanical and oxidation properties, Journal of Nuclear Materials 557 (2021). [doi:10.1016/j.jnucmat.2021.153272](https://doi.org/10.1016/j.jnucmat.2021.153272).
- 699 [16] L. He, M. Khafizov, C. Jiang, B. Tyburska-Püscherl, B. J. Jaques, P. Xiu, P. Xu, M. K.
700 Meyer, K. Sridharan, D. P. Butt, J. Gan, Phase and defect evolution in uranium-
701 nitrogen-oxygen system under irradiation, Acta Materialia 208 (2021). [doi:10.1016/j.actamat.2021.116778](https://doi.org/10.1016/j.actamat.2021.116778).
- 703 [17] J. C. Mauro, Materials Kinetics: Transport and Rate Phenomena, 1st Edition, Elsevier,
704 2020.
- 705 [18] T. Courtney, Mechanical Behavior of Materials, 2nd Edition, Waveland Press, Inc.,
706 2005.
- 707 [19] S. L. Hayes, J. K. Thomas, K. L. Peddicord, Material property correlations for uranium
708 mononitride III. transport properties, Journal of Nuclear Materials 171 (1990) 289–299.
- 709 [20] P. Kebbinski, D. Wolf, H. Gleiter, Molecular-dynamics simulation of grain-boundary
710 diffusion creep, Interface Science 6 (1998). [doi:10.1023/A:1008664218857](https://doi.org/10.1023/A:1008664218857).
- 711 [21] V. Yamakov, D. Wolf, S. R. Phillpot, H. Gleiter, Grain-boundary diffusion creep in
712 nanocrystalline palladium by molecular-dynamics simulation, Acta Materialia 50 (2002).
713 [doi:10.1016/S1359-6454\(01\)00329-9](https://doi.org/10.1016/S1359-6454(01)00329-9).
- 714 [22] T. G. Desai, P. C. Millett, D. Wolf, Molecular dynamics study of diffusional creep in
715 nanocrystalline UO₂, Acta Materialia 56 (2008). [doi:10.1016/j.actamat.2008.02.052](https://doi.org/10.1016/j.actamat.2008.02.052).
- 717 [23] C. O. Galvin, D. A. Andersson, R. T. Sweet, L. Capolungo, M. W. Cooper, Diffusional
718 creep model in UO₂ informed by lower-length scale simulations (2024).
- 719 [24] C. O. Galvin, D. A. Andersson, R. T. Sweet, L. Capolungo, M. W. Cooper, Diffusional
720 creep model in UO₂ informed by lower-length scale simulations, Journal of Nuclear Ma-
721 terials 607 (2025) 155659. [doi:https://doi.org/10.1016/j.jnucmat.2025.155659](https://doi.org/10.1016/j.jnucmat.2025.155659).
- 722 [25] A. J. Haslam, V. Yamakov, D. Moldovan, D. Wolf, S. R. Phillpot, H. Gleiter, Effects
723 of grain growth on grain-boundary diffusion creep by molecular-dynamics simulation,
724 Acta Materialia 52 (2004). [doi:10.1016/j.actamat.2003.12.048](https://doi.org/10.1016/j.actamat.2003.12.048).
- 725 [26] M. W. Cooper, K. A. Gamble, L. Capolungo, C. Matthews, D. A. Andersson, B. Beeler,
726 C. R. Stanek, K. Metzger, Irradiation-enhanced diffusion and diffusion-limited creep
727 in U₃Si₂, Journal of Nuclear Materials 555 (2021). [doi:10.1016/j.jnucmat.2021.153129](https://doi.org/10.1016/j.jnucmat.2021.153129).

- 729 [27] V. I. Tseplyaev, S. V. Starikov, The atomistic simulation of pressure-induced phase
730 transition in uranium mononitride, Journal of Nuclear Materials 480 (2016) 7–14. doi:
731 [10.1016/j.jnucmat.2016.07.048](https://doi.org/10.1016/j.jnucmat.2016.07.048).
- 732 [28] V. Kocevski, M. W. Cooper, A. J. Claisse, D. A. Andersson, Development and appli-
733 cation of a uranium mononitride (UN) potential: Thermomechanical properties and
734 Xe diffusion, Journal of Nuclear Materials 562 (2022). doi:[10.1016/j.jnucmat.2022.153553](https://doi.org/10.1016/j.jnucmat.2022.153553).
- 736 [29] M. AbdulHameed, B. Beeler, C. O. Galvin, M. W. Cooper, Assessment of uranium
737 nitride interatomic potentials, Journal of Nuclear Materials (2024) 155247 doi:<https://doi.org/10.1016/j.jnucmat.2024.155247>.
- 739 [30] M. AbdulHameed, B. Beeler, A. Claisse, Atomistic investigation of plastic deformation
740 and dislocation motion in uranium mononitride, Applied Sciences 15 (2025) 2666. doi:
741 <https://doi.org/10.3390/app15052666>.
- 742 [31] A. P. Thompson, H. M. Aktulg, R. Berger, D. S. Bolintineanu, W. M. Brown, P. S.
743 Crozier, P. J. in 't Veld, A. Kohlmeyer, S. G. Moore, T. D. Nguyen, R. Shan, M. J.
744 Stevens, J. Tranchida, C. Trott, S. J. Plimpton, LAMMPS—a flexible simulation tool for
745 particle-based materials modeling at the atomic, meso, and continuum scales, Computer
746 Physics Communications 271 (2022). doi:[10.1016/j.cpc.2021.108171](https://doi.org/10.1016/j.cpc.2021.108171).
- 747 [32] P. Hirel, Atomsk: A tool for manipulating and converting atomic data files, Computer
748 Physics Communications 197 (2015). doi:[10.1016/j.cpc.2015.07.012](https://doi.org/10.1016/j.cpc.2015.07.012).
- 749 [33] A. Stukowski, Visualization and analysis of atomistic simulation data with OVITO—the
750 open visualization tool, Modelling and Simulation in Materials Science and Engineering
751 18 (2010). doi:[10.1088/0965-0393/18/1/015012](https://doi.org/10.1088/0965-0393/18/1/015012).
- 752 [34] A. K. Mukherjee, An examination of the constitutive equation for elevated temper-
753 ature plasticity, Materials Science and Engineering: A 322 (2002). doi:[10.1016/S0921-5093\(01\)01115-7](https://doi.org/10.1016/S0921-5093(01)01115-7).
- 755 [35] N. Dowling, S. Kampe, M. Kral, Mechanical Behavior of Materials: Engineering Meth-
756 ods for Deformation, Fracture, and Fatigue, 5th Edition, Pearson Education Limited,
757 2020.
- 758 [36] R. L. Coble, A model for boundary diffusion controlled creep in polycrystalline materials,
759 Journal of Applied Physics 34 (1963). doi:[10.1063/1.1702656](https://doi.org/10.1063/1.1702656).
- 760 [37] Y. J. Wang, A. Ishii, S. Ogata, Transition of creep mechanism in nanocrystalline metals,
761 Physical Review B - Condensed Matter and Materials Physics 84 (2011). doi:[10.1103/PhysRevB.84.224102](https://doi.org/10.1103/PhysRevB.84.224102).
- 763 [38] D. R. Olander, A. T. Motta, Light Water Reactor Materials Volume I: Fundamentals,
764 American Nuclear Society, 2017.

- [39] A. Y. Kuksin, S. V. Starikov, D. E. Smirnova, V. I. Tseplyaev, The diffusion of point defects in uranium mononitride: Combination of DFT and atomistic simulation with novel potential, *Journal of Alloys and Compounds* 658 (2016) 385–394. [doi:10.1016/j.jallcom.2015.10.223](https://doi.org/10.1016/j.jallcom.2015.10.223).
- [40] S. L. Hayes, J. K. Thomas, K. L. Peddicord, Material property correlations for uranium mononitride IV. thermodynamic properties, *Journal of Nuclear Materials* 171 (1990) 300–318.
- [41] P. M. Larsen, Revisiting the common neighbour analysis and the centrosymmetry parameter (2020). [arXiv:2003.08879](https://arxiv.org/abs/2003.08879).
- [42] C. L. Kelchner, S. Plimpton, Dislocation nucleation and defect structure during surface indentation, *Physical Review B - Condensed Matter and Materials Physics* 58 (1998). [doi:10.1103/PhysRevB.58.11085](https://doi.org/10.1103/PhysRevB.58.11085).
- [43] V. Bulatov, W. Cai, *Computer Simulations of Dislocations*, Oxford University Press, 2006.
- [44] A. Stukowski, V. V. Bulatov, A. Arsenlis, Automated identification and indexing of dislocations in crystal interfaces, *Modelling and Simulation in Materials Science and Engineering* 20 (2012). [doi:10.1088/0965-0393/20/8/085007](https://doi.org/10.1088/0965-0393/20/8/085007).
- [45] W. Cai, W. Nix, *Imperfections in Crystalline Solids*, 1st Edition, Cambridge University Press, 2016. [doi:10.1017/cbo9781316389508](https://doi.org/10.1017/cbo9781316389508).
- [46] P. Kebinski, D. Wolf, S. R. Phillpot, H. Gleiter, Self-diffusion in high-angle FCC metal grain boundaries by molecular dynamics simulation, *Philosophical Magazine A: Physics of Condensed Matter, Structure, Defects and Mechanical Properties* 79 (1999). [doi:10.1080/01418619908212021](https://doi.org/10.1080/01418619908212021).
- [47] K. L. Murty, I. Charit, *An Introduction to Nuclear Materials*, 1st Edition, Wiley-VCH Verlag GmbH & Co. KGaA, 2013.
- [48] V. Yamakov, D. Wolf, M. Salazar, S. R. Phillpot, H. Gleiter, Length-scale effects in the nucleation of extended dislocations in nanocrystalline Al by molecular-dynamics simulation, *Acta Materialia* 49 (2001). [doi:10.1016/S1359-6454\(01\)00167-7](https://doi.org/10.1016/S1359-6454(01)00167-7).
- [49] R. S. Gordon, Ambipolar diffusion and its application to diffusion creep, *Materials Science Research* 9 (1974). [doi:10.1007/978-1-4684-3150-6_30](https://doi.org/10.1007/978-1-4684-3150-6_30).
- [50] M. Kizilyalli, J. Corish, R. Metselaar, Definitions of terms for diffusion in the solid state, *Pure and Applied Chemistry* 71 (1999). [doi:10.1351/pac199971071307](https://doi.org/10.1351/pac199971071307).
- [51] E. W. Hart, On the role of dislocations in bulk diffusion, *Acta Metallurgica* 5 (1957). [doi:10.1016/0001-6160\(57\)90127-X](https://doi.org/10.1016/0001-6160(57)90127-X).
- [52] A. A. Riet, J. A. V. Orman, D. J. Lacks, A molecular dynamics study of grain boundary diffusion in mgo, *Geochimica et Cosmochimica Acta* 292 (2021). [doi:10.1016/j.gca.2020.09.012](https://doi.org/10.1016/j.gca.2020.09.012).

- 802 [53] T. Arima, K. Yoshida, K. Idemitsu, Y. Inagaki, I. Sato, Molecular dynamics analysis
803 of diffusion of uranium and oxygen ions in uranium dioxide, IOP Conference Series:
804 Materials Science and Engineering 9 (2010).
- 805 [54] D. Prokoshkina, V. A. Esin, G. Wilde, S. V. Divinski, Grain boundary width, energy
806 and self-diffusion in nickel: Effect of material purity, Acta Materialia 61 (2013). [doi:10.1016/j.actamat.2013.05.010](https://doi.org/10.1016/j.actamat.2013.05.010).
- 808 [55] A. Cheniour, M. R. Tonks, B. Gong, T. Yao, L. He, J. M. Harp, B. Beeler, Y. Zhang,
809 J. Lian, Development of a grain growth model for U₃Si₂ using experimental data, phase
810 field simulation and molecular dynamics, Journal of Nuclear Materials 532 (2020). [doi:10.1016/j.jnucmat.2020.152069](https://doi.org/10.1016/j.jnucmat.2020.152069).
- 812 [56] Z. Zeng, Y. Pan, X. Chen, C. Zhang, C. Yin, S. Gao, Y. Zhou, J. Zhang, X. He, C. Yuan,
813 Three-dimensional modeling of thermal-mechanical behavior of accident tolerant fuels,
814 Frontiers in Energy Research 9 (2021). [doi:10.3389/fenrg.2021.636502](https://doi.org/10.3389/fenrg.2021.636502).
- 815 [57] E. W. Weisstein, [Truncated octahedron](#), MathWorld: A Wolfram Web Resource.
816 URL <https://mathworld.wolfram.com/TruncatedOctahedron.html>